Journal of Materials Chemistry A

PAPER

View Article Online
View Journal | View Issue

Cite this: J. Mater. Chem. A, 2019, 7, 25333

Carbon fibre paper coated by a layered manganese oxide: a nano-structured electrocatalyst for water-oxidation with high activity over a very wide pH range†

Jens Melder, [a] Stefan Mebs, [b] Philipp A. Heizmann,[a] Rebekka Lang,[a] Holger Dau *[b] and Philipp Kurz *[a]

Manganese oxide coated carbon fibre paper electrodes (MnO_x/CFP), prepared *via* an easily scalable redox-deposition route, have been reported as promising materials for electrochemical water oxidation catalysis (WOC). In the study presented here, the catalyst mass-dependence of the activity of such nanostructured WOC electrodes and their activity and stability in phosphate buffer electrolytes over nearly the entire pH range (pH 1–14) was explored. For all pH values, current densities of >1 mA cm^{-2} at overpotentials η of 350–500 mV were observed, which are very good values for electrodes containing only earth-abundant elements (Mn, O and C in this case). The very decent performance observed for the mildly acidic pH regime (pH 2–6) was especially noteworthy. For the dependence of η on the pH, an ideal Nernstian behaviour was detected for the pH window pH 1–10. Above pH 10, a pronounced deviation from the expected trend was found, as most electro-kinetic parameters indicated even higher activities for the strongly alkaline regime. Concerning anode stabilities, current-densities of 2 mA cm^{-2} could be maintained at all studied pHs over at least 24 h of continuous operation. Pre- and post-*operando* spectroscopic analyses (*e.g.* vibrational and X-ray absorption spectroscopy, scanning electron microscopy) revealed only minor changes of the catalyst structure, composition, morphology or the average Mn oxidation state induced by the electrocatalytic operation, which confirms the good stabilities found in the electrochemical measurements. Thus, we report on an earth-abundant, easily-prepared type of WOC electrode, which exhibits promising activities and stabilities for applications in alkaline, neutral and even acidic electrolytes.

Received 12th August 2019
Accepted 12th October 2019

DOI: 10.1039/c9ta08804k

rsc.li/materials-a

Introduction

The electrochemical splitting of water to hydrogen and oxygen with earth-abundant, non-toxic catalysts (*e.g.* Mn or Fe) is a promising pathway to efficient and durable solar energy conversion and storage systems.[1–4] Of the two half reactions for water splitting, the oxygen evolution reaction (OER) can still be seen as a major bottleneck for the overall process since the reaction is kinetically very demanding due to the coupled transfer of four protons and four electrons for the generation of one oxygen molecule (eqn (1)).[5–7]

The minimum potential necessary to drive this reaction is +1.23 V *vs.* the reversible hydrogen electrode (RHE). However, high overpotentials η (often >400 mV for precious metal free catalyst systems) need to be applied to achieve reasonable current densities.

$$2H_2O_{(l)} \rightarrow O_{2(g)} + 4H^+_{(aq)} + 4e^- \quad (1)$$

The OER overpotentials depend on several parameters, most important amongst them the exact composition, modification and morphology of the electrocatalyst, the support material used to fabricate the anodes and also the electrolyte (pH, dissolved ions, concentrations *etc.*).[8] In alkaline media, for example, a plethora of precious and non-precious metal oxide catalysts with high activities and corrosion stabilities are known and used in commercial alkaline electrolysis cells for water splitting up to the megawatt range.[9–11] As an example for the very good OER performance at high pH, some mixed Ni/Fe oxides can reach j = 10 mA cm^{-2} for η < 300 mV in 1 M KOH.[12–14] Significant progress has also been made in the

[a]Institut für Anorganische und Analytische Chemie, Freiburger Materialforschungszentrum (FMF), Albert-Ludwigs-Universität Freiburg, Albertstraße 21, 79104 Freiburg, Germany. E-mail: philipp.kurz@ac.uni-freiburg.de

[b]Fachbereich Physik, Freie Universität Berlin, Arnimallee 14, 14195 Berlin, Germany. E-mail: holger.dau@physik.fu-berlin.de

† Electronic supplementary information (ESI) available: Experimental details, electrochemical measurements and additional figures and tables with results from electrochemistry, XAS, UV/Vis, AAS, SEM, EDX, Raman and XRD. See DOI: 10.1039/c9ta08804k

development of water oxidation catalysis (WOC) at near neutral conditions. This field has received a boost in 2008, when Kanan and Nocera reported on a self-healing, low-cost cobalt oxide OER catalyst with promising WOC activity at pH 7 ($j \sim 1$ mA cm^{-2} for $\eta < 450$ mV).[6] Since then, numerous other noble-metal free OER catalysts have been developed, mainly based on Co,[15] Ni,[16,17] Fe[18,19] or Mn[20–22] oxides and often also operated in neutral electrolytes. In comparison, the only convincing materials for WOC in acidic media are based on the scarce and therefore expensive and hardly scalable elements Ru and Ir,[23,24] while especially Ni and Co based electrodes suffer from corrosion and show little activity.[25,26]

Thus, the development and optimization of earth abundant OER electrocatalysts which are stable in neutral to acidic media remains a challenge in order to *e.g.* further improve (photo-) electrochemical devices such as artificial leaves or polymer electrolyte membrane (PEM) electrolysers, which are operated at pH $\leq$ 7 to avoid corrosion issues and/or due to performance limitations of the applied membranes.[27,28]

The oxygen evolving complex (OEC) of the enzyme Photosystem II is a $Mn_4CaO_5(H_2O)_x$-cluster, and with it biology provides a template for a highly efficient water oxidation catalyst in neutral media (TOF of about 300 O_2 per s at $\eta = \sim$300 mV, pH 5.5 (ref. 29)) that is composed only of earth-abundant elements.[30–33] Here, the accumulation of the four oxidation equivalents needed for the OER according to eqn (1) is mainly accomplished by Mn ions switching between the oxidation states +III and +IV coupled to deprotonation steps of coordinated water molecules or hydroxide ions.[34,35] As a consequence, many manganese oxide (MnO_x) polymorphs have been synthesized and screened for their WOC activity, with the result that amorphous manganese oxides with layered or tunnelled structures often show the best performances, especially in neutral to acidic reaction media.[36–43] Prominent examples for such manganese oxide catalysts belong to the mineral family of birnessites, which contain layers of edge-sharing [MnO_6]-octahedra with a layer to layer distance of approximately 7 Å. Similar to many clay materials, the interlayer space is occupied by varying amounts of water and additional cations (especially of the alkali and alkaline earth metals), so that a nearly unlimited variety of birnessite compositions is possible. Additionally, the average manganese oxidation state in birnessites is also flexible within a rather wide range between ~+3.3 and ~+3.9.[37,44]

As manganese oxides generally possess only mediocre electric conductivities, it is necessary to deposit the prospective MnO_x catalysts on conductive supports in order to obtain functional anodes for WOC. This can be achieved *via* several methods including electrodeposition, screen-printing, spin-coating or spray-coating.[20,21,45–47] Recently, some of us developed a rather unusual synthetic procedure to directly coat different carbon supports with birnessite-type MnO_x using an *in situ* redox deposition where the carbon itself acts as reducing agent for $KMnO_4$ in acidic aqueous solution.[22] Unlike many other methods, no additional macromolecular binders like Nafion or polyethylene oxide (PEO) are needed to achieve stable oxide coatings. Electrochemical tests of four different types of such "MnO_x/C-electrodes" showed very promising OER activities and corrosion stabilities in a neutral, phosphate-buffered electrolyte, especially when the catalyst layers where deposited on sp^2-rich, nanostructured carbon supports like carbon fibre paper (CFP). After some optimization steps, our best MnO_x/CFP-anodes reached current densities of 1 mA cm^{-2} at pH 7 and $\eta \sim$ 450 mV for at least 16 h.[22] These anodes are thus at least as active and stable in neutral media as "Nocera-type" CoO_x analogues, but are now based on the again much cheaper and non-toxic metal manganese (~2 € per kg(Mn) *vs.* ~23 € per kg(Co)).[48]

Here, we now present the results of an extensive study of the electrochemical activities and stabilities of MnO_x/CFP-electrodes over nearly the full pH range ($1.5 \leq$ pH ≤ 14.0) to assess the usability of such anodes for other pH-regimes. Moreover, detailed electro-kinetic measurements were carried out to elucidate the pH dependence of OER catalysis by MnO_x and the influence of the concentration of the buffering electrolyte on the OER rate. Additionally, the dependence of the activity with respect to the catalyst mass was investigated and extensive pre- and post-*operando* characterizations were carried out by means of ATR-IR-, Raman-, X-ray absorption-spectroscopy (XAS), XRD, SEM, EDX and elemental analyses using AAS.

Experimental

Materials

Graphitized carbon fibre paper (CFP, TGP-H-60), was purchased from Toray Carbon Inc., cut into pieces of 1 × 2 cm^2 and pre-treated by sonication for 15 min. each in 0.1 M HNO_3, ethanol and water, respectively. Please consult the ESI† for further details concerning the materials used for this study.

Preparation of MnO_x/CFP-electrodes

The preparation of MnO_x/CFP-electrodes using the *in situ* redox reaction between permanganate and carbon has been described in detail elsewhere.[22] In short, 2.5 mL of HNO_3 (69%) were added to a beaker containing a $KMnO_4$-solution (0.1 M, 100 mL) and the strongly acidic mixture (pH ~ 0.4) was then heated to 70 °C. Subsequently four pre-treated pieces of CFP were dipped into the slowly stirred solution simultaneously. To ensure that only 1 cm^2 of the carbon material was exposed to the solution, the rest of the area was covered with adhesive tape (tesafilm®, "matt-unsichtbar", thickness ~70 μm). This step was carried out for different times (15–360 min) in order to obtain different thicknesses of the MnO_x layer. The electrodes were then taken out of the $KMnO_4$ solution, washed thoroughly with water, dried in air at 60 °C for 1 h and finally calcined in a muffle furnace in air at a temperature of 400 °C for 1 h.

Instrumental methods

Details of the instrumentation and measurement conditions used to record vibrational spectra (ATR-FT-IR and Raman), electron micrographs (SEM), energy dispersive X-ray analyses (EDX), *in operando* UV/Vis-spectroscopy, X-ray powder

diffractograms (XRD), X-ray absorption spectra (XAS) and for the determination of potassium or manganese fractions by flame atomic absorption spectroscopy (AAS) are provided in the ESI.†

Electrochemical measurements

All electrochemical experiments were conducted in a typical three-electrode setup using a VersaStat 4 potentiostat/galvanostat (Princeton Applied Research) with an integrated module for electrochemical impedance spectroscopy (EIS). The electrochemical cell (volume 100 mL) typically consisted of a Ag/AgCl reference electrode (Metrohm, 3 M KCl, +0.207 V *vs.* NHE at 25 °C), a Pt rod as counter electrode (Metrohm, diameter ~2 mm) and MnO_x/CFP as working electrodes (WE). All measurements were conducted in 50 mL of the respective air-saturated electrolyte at ambient temperature (~23 °C) and WE potentials were converted to RHE according to eqn (2).

$$E_{RHE} = E_{Ag/AgCl} + 0.207 + 0.059pH \text{ (in V)} \quad (2)$$

To evaluate the electrocatalytic behaviour of the MnO_x/CFP-anodes for water-oxidation in different electrolytes, a multi-step protocol consisting of the determination of the uncompensated resistance R_u (by EIS), cyclic voltammetry sweeps (CV, three cycles), "staircase" chronoamperometry measurements (CA, for the determination of Tafel plots) and again cyclic voltammetry sweeps (three cycles) over a wide potential range was used (see ESI for details†). To minimize the possibility of mass transport limitations and the formation of a pH gradient in the pores of the catalyst, the solutions were stirred during the CA measurements. In staircase CA-protocols, potentials were held constant for 5 min at each step in order to exclude a large contribution of the capacitive current to the overall current density. The average current density over the last 30 s of each step was then used for Tafel-analyses. To evaluate the long-term stability of MnO_x/CFP under different electrolyte conditions, chronopotentiometry measurements (CP) at current-densities of 2 mA cm^{-2} were performed for a duration of 24 h. All CA, CP and CV measurements were *iR*-corrected at 85%.

Details for the preparation of the different potassium phosphate buffer electrolytes are listed in the ESI.†

Results and discussion

Synthesis of MnO_x/CFP electrodes and catalyst mass dependence of WOC rates

The MnO_x/CFP electrodes obtained from the *in situ* redox deposition reaction followed by a 1 h calcination step at 400 °C feature a uniform MnO_x coating of the carbon substrate. As a result of the preparation conditions (acidic $KMnO_4$ solutions), the oxide also contains K^+-ions and can thus be identified as a K-birnessite, which is in agreement with XAS-, ATR-IR-, XRD- and Raman data (see Fig. 3–5 below and ref. 22).

For a determination of the amounts of the deposited Mn and K ions, the oxide layer was completely dissolved in a mixture of H_2O_2 and HNO_3 and the resulting solution was then analysed by AAS. We found that the deposited amounts of Mn and K depend linearly on the deposition time, while the detected molar K : Mn-ratio has a virtually constant value of ~0.09 : 1 for all samples (see ESI, Fig. S1†).

The dependence of the catalytic activity of the MnO_x/CFP electrodes per geometric area and per number of Mn-ions with respect to deposition-time was identified by stepwise chronoamperometry (CA) measurements in 0.4 M potassium phosphate buffer (KP_i, pH 7), which were subsequently translated into Tafel plots (see ESI, Fig. S2†). For $\eta = 450$ mV, a steady, about six-fold increase of the current density as a function of the deposited amount of birnessite catalyst from $j \sim 0.5$ mA cm^{-2} for an electrode functionalized for 30 min to $j \sim 3$ mA cm^{-2} for one immersed for 6 hours could be extracted from these plots (Fig. 1a, purple bars). When the current densities are normalized to the number of Mn ions, the specific activity per μmol(Mn) decreases with the amount of deposited catalyst to less than half from ~0.5 to ~0.2 mA per μmol(Mn) (Fig. 1a, green bars; see Fig. S3 in the ESI† for the corresponding Tafel plots). The observed increase of j_{geom} with the mass loading indicates that the catalytic reaction does not only take place at the outer surface of the MnO_x catalyst layer, but also within the oxide material, which from previous studies is known to be mesoporous.[49] However, for higher loadings the activity per manganese decreases, most probably because the fraction of material at the bottom of the catalyst volume can contribute less and less to the reaction due to mass-transport limitations while in parallel the low electric conductivity of the MnO_x also limits the performance of the top of the catalyst layers. Macroscopic diffusion processes limiting proton transport between anode and cathode could also contribute.[50]

To further evaluate this behaviour, Fig. 1b shows the logarithm of the current density against the logarithm of the number of Mn-ions for different overpotentials (again extracted from the Tafel-plots shown in Fig. S2†). The current density depends linearly (near unity slope) on the number of deposited Mn-ions for loadings of 0.2–2 μmol(Mn) per cm^2. At high loadings *and* high current densities (*i.e.* large η), a distinct flattening of the curve is observable.

Overall, this indicates that an increase of the catalytic activity by raising the catalyst mass loading is generally possible, but only to a limited extent – a trend which our groups have already observed previously for screen-printed layers of a Ca-birnessite catalyst on a conductive oxide support.[21] Additionally, long-term activity *and* stability measurements (chronopotentiometry in 0.4 M KP_i, pH 7 at $j = 2$ mA cm^{-2} for 24 h) for the same set of anodes also show a certain "upper limit" of WOC activities for increasing MnO_x loadings (Fig. S4†). Looking at the complete dataset, we identify MnO_x/CFP-electrodes with a mass loading of ~3 μmol(Mn) per cm^2 (functionalisation time 90 min) as the best of our series. These are able to reach a stable current density of 2 mA cm^{-2} at $\eta \sim 480$ mV after 24 h.

From theory and as shown by many studies on metal oxides before, the electrical capacitance is predicted to increase with increasing contact area between the oxide catalyst and the electrolyte, giving a good estimate of the surface area of an electrocatalyst.[23,51–53] However, a reliable calculation of the surface area from the measured double layer capacitance

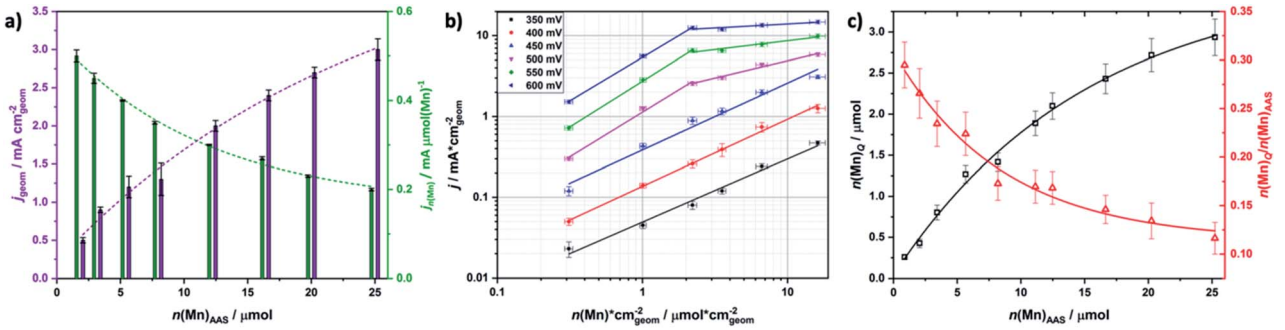

Fig. 1 (a) OER current densities for MnO_x/CFP electrodes functionalized for different times normalized to the geometric surface area (purple bars) and to the number of deposited manganese ions (green bars) at an overpotential $\eta = 450$ mV. The dashed lines are shown to guide the eye and were calculated assuming an exponential asymptotic increase of j_{geom} and an exponential decrease of $j_{n(Mn)}$; (b) double logarithmic representation of the OER current densities as a function of the amount of deposited manganese ions for six different overpotentials ranging from 350 mV to 600 mV; (c) amount of manganese ions undergoing redox-changes ($n(Mn)_Q$, black open square) during the CVs shown in Fig. S3† for electrodes functionalized for different times. $n(Mn)_Q$ was calculated by integration of the negative cathodic currents in Fig. S3.† The resulting charge Q was afterwards divided by the Faraday constant F to calculate the amount of redox active manganese ions. Please note that this calculation is based on the assumption that the dominating redox active manganese species during OER are Mn^{3+} and Mn^{4+}. The fraction of oxidizable manganese ions ($n(Mn)_Q/n(Mn)_{AAS}$) was calculated by dividing $n(Mn)_Q$ by the amount of manganese ions per electrode determined by AAS ($n(Mn)_{AAS}$, red open triangle). The lines are shown to guide the eye and were calculated assuming an exponential asymptotic increase of $n(Mn)_Q$ and an exponential decrease of $n(Mn)_Q/n(Mn)_{AAS}$. Conditions: 0.4 M potassium phosphate buffer; pH 7. The error bars represent 1σ.

proved to be impossible in our case. Amorphous manganese oxides are widely known as electrochemical capacitors (and even supercapacitors), as they exhibit very large pseudo-capacitances due to faradaic redox reactions during charging/discharging (compare structured pre-wave in the CVs of Fig. S5 in the ESI†).[54,55] For MnO_x/CFP electrodes, these non-catalytic redox waves are usually explained by oxidation/reduction reactions of the Mn ions in the material.[20,54,56,57] Consequently, an integration of the negative currents of the cathodic scan in the CV can be used as a good estimate for the number of manganese ions undergoing redox-changes during a CV cycle. The result of this integration is a reduction charge Q, which, divided by the Faraday constant F (and assuming single-electron redox reactions for Mn only, most likely $Mn^{3+} \leftrightharpoons Mn^{4+}$), leads to the molar amount of redox active Mn ions $n(Mn)_Q$. As shown in Fig. 1c (black trace), longer deposition times (and thus thicker MnO_x layers) lead to an increase of $n(Mn)_Q$. However, this increase again seems to approach a certain limit and interestingly, the shape of the curve closely resembles that shown above for the variation of the geometric current density j_{geom} *versus* the deposition time (Fig. 1a, purple bars). Hence, the amount of manganese ions showing an ability to undergo redox-changes during a CV scan seems to be linked to the water oxidation activity of MnO_x/CFP.

In addition, it is also possible to calculate the fraction of redox active manganese ions by dividing $n(Mn)_Q$ by the total amount of deposited manganese determined by AAS ($n(Mn)_{AAS}$). The fraction $n(Mn)_Q/n(Mn)_{AAS}$ changes profoundly from about 28% (low loadings) to ~12% (high loadings). Again this trace shows a great similarity to the plot of current density per deposited Mn ($j_{n(Mn)}$) *versus* oxide loading (Fig. 1a, green bars).

Both trends visible in Fig. 1c are therefore in very good agreement with the previous analysis of the data shown in Fig. 1: (1) the increase of the fraction of oxidizable manganese ions $n(Mn)_Q$ at higher loadings again indicates that catalysis also takes place within the "bulk" of the MnO_x coatings and (2) the decrease of the fraction of redox active manganese ions at higher loadings shows that the average activity per manganese ion is lowered, meaning that not all Mn^{n+} contribute equally to the activity of the electrode.

To conclude, MnO_x/CFP reveals characteristics of a volume catalyst, as the activity of the catalyst layer is over a wide range proportional to the amount of deposited MnO_x material. Analysis of CV waves assignable to Mn oxidation state changes further indicate that the entire volume of the porous oxide is accessible for water and ions from the electrolyte, even for high catalyst loadings. However, the addition of more and more birnessite will likely lead to the problem of lower conductivity as well as transport limitations due to a hindered removal of O_2 gas and/or H^+ from the catalytic sites. A similar behaviour was also observed for other porous catalyst systems, *e.g.* CoP_i.[58] Additionally, the low electric conductivity of manganese oxides could also contribute to this effect, rendering sites far away from the carbon support less active than those close by.[59]

Electrocatalytic activity at different pH

Next, we studied water oxidation electrocatalysis by MnO_x/CFP at three different pH values (2.5, 7.0 and 12.0, roughly corresponding to the three pK_a values of phosphoric acid). In each case, buffers containing a total phosphate concentration of 1.0 M served as electrolytes and the MnO_x/CFP anodes used were of the optimal catalyst layer thickness determined in the previous experiments (~3 µmol(Mn) per cm^2, functionalisation time 90 min). At this point it is necessary to mention that phosphate buffers exhibit different ionic conductivities σ for different pH values which are related to the uncompensated solution resistance R_u of the electrolyte (see Table 1). This could significantly influence the measurements (especially for higher

Table 1 Ionic conductivities σ of the electrolytes, electrolyte resistance R_u, Tafel-slopes, overpotentials η needed to achieve current densities of 1 or 5 mA cm^{-2} (extracted from the Tafel plots in Fig. 2b), η after 24 h of operation at an applied current density of 2 mA cm^{-2} (extracted from Fig. 2c) for MnO_x/CFP-electrodes at different pH-values and number of deposited Mn-ions for MnO_x/CFP-electrodes before and after as well as number of Mn-ions found in the electrolyte after 24 h of electrolysis at an applied current density of 2 mA cm^{-2} determined by AAS-measurements

	σ [mS cm^{-1}]	R_u [Ω]	Tafel-slope [mV dec^{-1}]	η @ 1 mA cm^{-2} [mV]	η @ 5 mA cm^{-2} [mV]	η after 24 h of operation @ 2 mA cm^{-2} [mV]	n(Mn) for MnO_x/CFP before electrolysis[a] [μmol cm^{-2}]	n(Mn) for MnO_x/CFP after 24 h electrolysis[a] [μmol cm^{-2}]	n(Mn) in the electrolyte after 24 h electrolysis[a] [μmol cm^{-2}]
pH 2.5	51	5.8	135	455	550	515	3.2 ± 0.3	3.0 ± 0.2	0.1 ± 0.1
pH 7	95	3.4	110	445	525	500	3.0 ± 0.1	2.8 ± 0.1	0.1 ± 0.1
pH 12	122	2.8	55	360	405	420	3.1 ± 0.1	3.0 ± 0.2	—

[a] All values are the average of two individual measurements.

current densities) and therefore all applied potentials were corrected for ohmic losses (*iR*-drop) by a determination of R_u by electrochemical impedance spectroscopy (EIS). With this data, all electrochemical measurements were *iR*-corrected at 85% and potentials were converted to the RHE-scale using eqn (2).

Fig. 2a shows cyclic voltammograms for the potential range of 1.2–2.0 V *vs.* RHE for the three investigated pH values. Two distinct regions, typical for Ni-, Co- or Mn-oxide electrodes, can be identified in the CVs: (1) broad, unresolved, pseudo-capacitive redox waves between 1.2 and 1.6 V (see also inset in Fig. 2a). As already mentioned above, these are most likely caused by $Mn^{3+} \rightarrow Mn^{4+}$ redox transitions in combination with the insertion/removal of H^+ (or K^+) from/to the electrolyte according to eqn (3).[20,60]

$$MnO_{x-\delta}(OH)_{y+\delta(s)} \leftrightharpoons MnO_x(OH)_{y(s)} + \delta H^+/K^+_{(aq)} + \delta e^- \quad (3)$$

(2) A more pronounced reductive feature between 1.5 V and 1.2 V during the cathodic scan. A slight shift of the minimum of

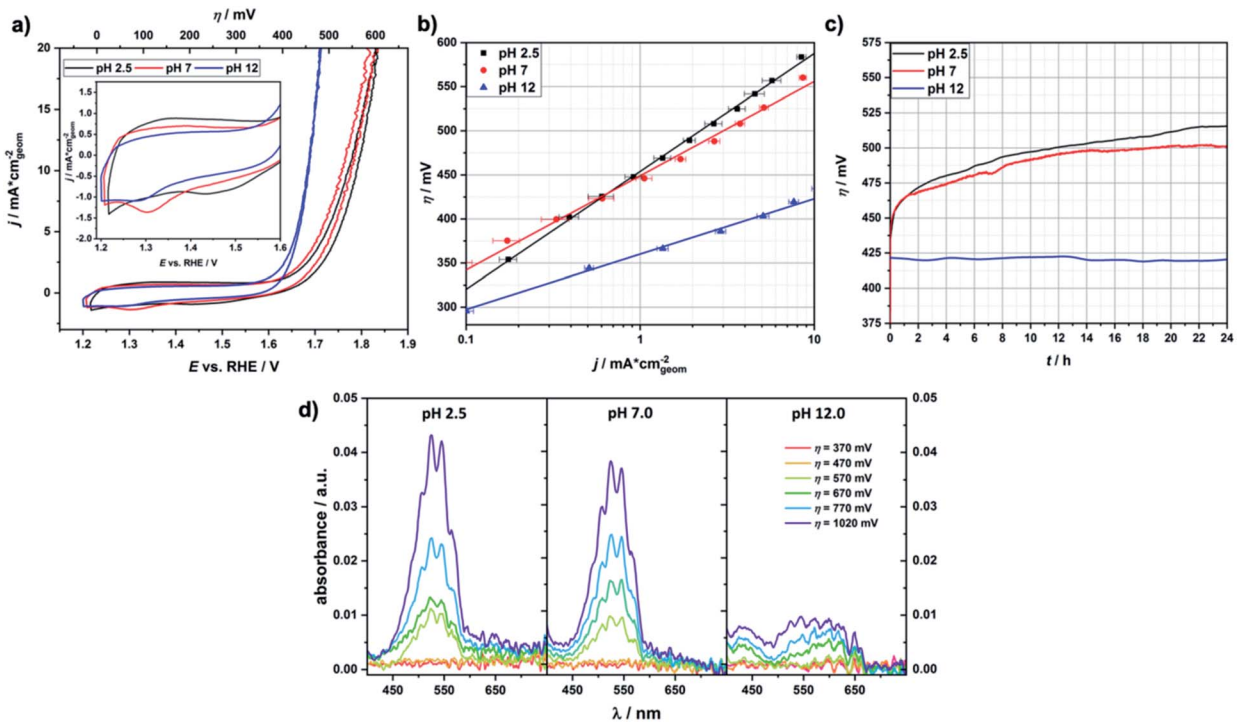

Fig. 2 (a) Cyclic voltammograms for MnO_x/CFP-electrodes in 1 M KP_i-buffer at pH 2.5/7.0/12.0 (in each case the 3rd CV cycle is plotted). The inset shows a magnification of the pseudo-capacitive potential region; (b) Tafel-plots (from staircase CA experiments, see Fig. S6†) for the same anodes and electrolytes showing a linear log *j vs.* η relationship over two orders of magnitude of current density; (c) chronopotentiometric long-term activity/stability measurements for the same anodes and electrolytes at a constant current-density of j = 2 mA cm^{-2} for 24 h; (d) *in operando* UV/Vis-absorption difference spectra of the 1 M KP_i-electrolytes after 30 min of electrolysis at the indicated potentials. All shown traces are the average of two individual measurements. The error bars represent one standard deviation.

this peak with pH can be seen (from ~1.28 V for pH 12.0 to ~1.45 V for pH 2.5). Earlier work has assigned this event also to $Mn^{4+} \rightarrow Mn^{3+}$ redox transitions[20,54,56,57] and (3) an irreversible oxidation wave for $E >$ ~1.6 V, indicating the onset of catalytic water oxidation. The overpotential at which this catalytic OER current reaches 1 mA cm^{-2} decreases from $\eta \sim 400$ mV (for pH 2.5) to $\eta \sim 380$ mV (pH 7.0) and further to $\eta \sim 340$ mV (pH 12.0). Thus basic conditions generally facilitate WOC by MnO_x/CFP-anodes – similar to OER electrocatalysis by other 3d-metal oxides.[23]

In Fig. 2b, Tafel-plots for the three pH-regimes are shown. In all cases, a nearly ideal linear dependence of log(*j*) *vs.* *E* was found for the current-density range of 0.1–10 mA cm^{-2}. A linear regression revealed a pronounced decrease of the Tafel slopes *b versus* pH (see Table 1), which again indicates that the kinetic WOC rate for MnO_x/CFP-electrodes is higher under alkaline conditions than in neutral or acidic media. From a mechanistic point of view, a change of the rate determining step (RDS) under different pH-conditions can be assumed, which we will discuss in more detail later in this work.

For a possible use as OER-electrodes in technical applications, the long-term stabilities/activities of the anodes is of great importance. Therefore, the MnO_x/CFP-electrodes were tested in chronopotentiometric measurements at a constant current density of 2 mA cm^{-2} over 24 h at the three pH conditions. The resulting η *vs.* *t* traces are shown in Fig. 2c. After 24 h of operation, the electrodes tested under alkaline conditions need ~80–90 mV less overpotential to reach the set current density in comparison to the ones used in neutral or acidic media (Table 1). Even though the initial η's are very similar ($\eta \sim 430$ mV), significant increases of the η's by ~50 mV were found for the electrodes tested at pH 7.0 and pH 2.5 during the first ~3 h of the experiments. After this, a constant, but much slower growth is observed for the rest of the experiment. In contrast, the overpotential needed to drive the OER was nearly constant over the whole time of the experiment for electrodes tested under basic conditions.

In order to clarify possible reasons for the instability of MnO_x/CFP under acidic to neutral pH conditions, we measured UV/Vis-spectra of the 1 M KP_i-electrolytes (pH 2.5/7.0/12.0) after 30 min of electrolysis at different overpotentials of $370 < \eta <$ 1020 mV (see Fig. 2d). For pH 2.5 and 7.0 and $\eta >$ ~570 mV, these spectra show the very characteristic absorption peaks assignable to MnO_4^- for the spectral region around 450–540 nm.[61] Permanganate formation has recently also been observed by Li *et al.* for γ-MnO_2-electrodes operated at pH 2 and potentials above ~1.8 V ($\eta \sim 570$ mV). In contrast, only a very small absorption peak is visible for the electrode used for electrolysis at pH 12.0 even for the highest applied overpotentials of $\eta \sim 1020$ mV. Accordingly, the slow decay of activity observed if MnO_x/CFP is operated in acidic or neutral media might occur *via* a route involving permanganate as an intermediate and that this seems to be blocked under alkaline conditions.

To investigate the formation of MnO_4^--ions in electrolytes of pH 2.5 and 7.0 in more detail, UV/Vis-spectra were recorded at 15 min-intervals during CA-experiments at a constant potential of 1.8 V for 3.5 h (see ESI, Fig. S7†). After 30 min of electrolysis, the permanganate absorption peaks are clearly visible for both pH values with a measured absorption of Abs ~0.04. Over the following 60 min of electrolysis, the intensity of this signal increases only slightly to maximal absorbances of ~0.05 (pH 7.0) and ~0.06 (pH 2.5). According to the Beer–Lambert law, less than 1% of the total Mn-content per electrode is thus oxidized to permanganate (assuming a molar absorptivity coefficient $\varepsilon = 2300\ M^{-1}\ cm^{-1}$ at $\lambda = 525$ nm). After that, no further growth is discernible indicating that the permanganate concentration has reached a kind of saturation. This might be explained by two different scenarios: (1) permanganate formation occurs only in the first hours of electrolysis or (2) permanganate formation and follow-on reactions of MnO_4^- are in equilibrium. Interestingly, we did not find a permanganate signal any more if the electrolytes were allowed to stand for *ca.* 15 min after the end of the CA-experiments with no potential applied. Therefore, the second scenario mentioned above seems more likely.

Finally, we checked whether dissolved manganese can be detected in the electrolyte after electrolysis using AAS (Table 1). The AAS-results reveal that only a small fraction of the Mn (<5% for pH 2.5 and 7.0 within the standard variance of the measurement) are leached into the electrolyte during 24 h of electrolysis. It is therefore possible, that MnO_x/CFP undergoes a dissolution/re-deposition process in which MnO_4^- reacts with the remaining oxide to be reduced back to MnO_x (possibly oxidizing water in the process). However, the fresh MnO_x surface layer formed in this way seems to be less active than the original one, leading to the observed increase of the overpotential over the duration of long-term CP-experiments.

Despite the slow loss of activity, the behaviour of the MnO_x/CFP-electrode at pH 2.5 is surprising, since the overall activity at this low pH (even though lower than under alkaline conditions) is still very good compared to other catalyst systems with manganese as the only catalytically active metal. For example, it has been reported that MnO_x-based electrodes formed by successive electrodeposition steps at different potentials exhibited overpotentials of $\eta \sim 500$ mV at 200 μA cm^{-2} in pH 2.5 phosphate buffer.[62,63] Furthermore, other noble-metal free systems are either unstable under acidic conditions (Co- or Ni-oxides) or show much higher overpotentials. As two examples, $\eta \sim 820$ mV at 10 mA cm^{-2} and pH 2.2 have been reported for Co/Fe-Prussian blue compounds[64] and $\eta \sim 745$ mV at 10 mA cm^{-2} and pH 0 for $Ni_{0.5}Mn_{0.5}Sb_{1.7}O_x$ – both much worse than the $\eta \sim$ 600 mV at 10 mA cm^{-2} and pH 2.5 found here for MnO_x/CFP. However, it should also be mentioned that the values for MnO_x/CFP for acidic media are still 300–400 mV worse than those of the most active Ir-based OER catalysts, where *e.g.* values like $\eta =$ 270–290 mV at 10 mA cm^{-2} and pH 0.3 for $IrO_x/SrIrO_3$ can be found in the literature.[65]

To summarize, we would like to stress that our MnO_x/CFP WOC anodes show a surprisingly good performance in acidic phosphate electrolytes of pH 2.5 and can easily compete with the OER activities of other Mn-,[20,21,45,47,66,67] Co-,[18,68] Fe-[18] or Ni-[25] oxides at neutral conditions. The same is true for a comparison with other MnO_x- and CoO_x-based systems in alkaline media,[62,69] while the exceptional activities of $FeNiO_x$-catalysts in

strongly alkaline media are clearly not reached by MnO_x/CFP.[10,70–72]

Post *operando* characterization of electrodes after operation at different pH

In order to determine morphological or structural changes that could explain the different behaviour of the catalysts for the different pH regimes, various analytical measurements were carried out for the as-prepared electrodes (sometimes even before the sintering step at 400 °C) and compared to *ex situ* post-*operando* studies after 24 h of continuous operation at $j = 2$ mA cm^{-2} in 1 M phosphate electrolytes of pH 2.5, 7.0 and 12.0.

First, possible changes of the surface morphologies due to long-term electrochemical water-oxidation were examined by SEM (Fig. 3 and ESI, Fig. S8†). The preparation method yields carbon fibres uniformly covered by the manganese oxide in form of a highly disordered, sponge-like structure which is typical for birnessites.[20,36,45] After 24 h of OER-electrocatalysis, no significant differences of this structure compared to the original electrode is visible, indicating that no major morphological changes of the birnessites catalyst seem to occur during electrolysis at neither of the three investigated pH values. Furthermore, no cracks in the layers or losses of material are visible. In a former study we found that less graphitic carbon substrates can corrode at OER potentials even in neutral electrolytes.[22] The SEM images recorded here show that this does not seem to be a major problem for CFP as support material – even at alkaline or acidic conditions.

In all cases, the ATR-IR-spectra (Fig. 4) show prominent bands between 500–750 cm^{-1} (vibrations of [MnO_6]-octahedra[22,36,73]) and broad absorptions between 3000–3600 cm^{-1} and 1500–1700 cm^{-1} (O–H stretching and deformation vibrations of OH^- and/or H_2O).[74] In addition, the spectra recorded after electrochemistry reveal two broad features centred around

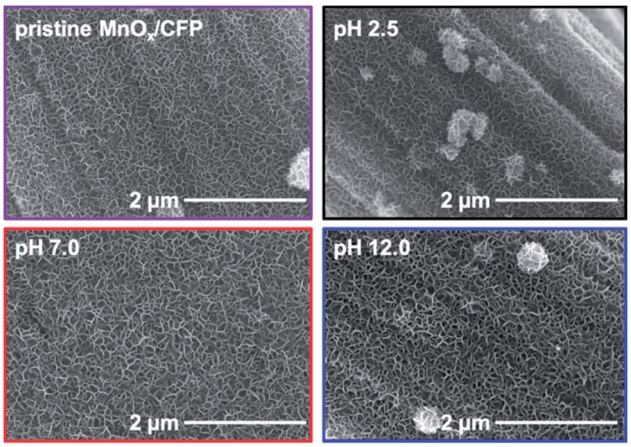

Fig. 3 SEM micrographs of the catalyst layers of an as prepared MnO_x/CFP-electrode (purple frame) and MnO_x/CFP-electrodes treated for 24 h at a constant current density of $j = 2$ mA cm^{-2} in 1 M KP_i-buffers of pH 2.5 (black), pH 7.0 (red) and pH 12.0 (blue), respectively at a magnification of ×25 000. Additional XRD-, Raman- and SEM-measurements can be found in Fig. S8–S14 of the ESI.†

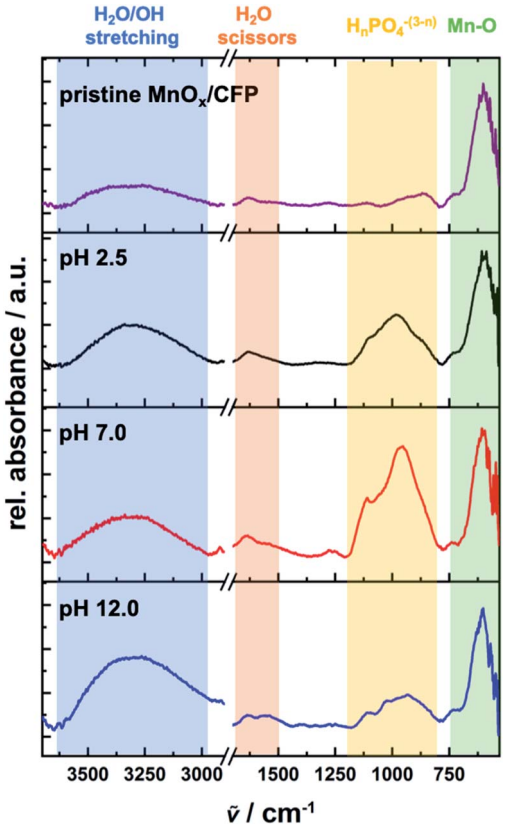

Fig. 4 ATR-IR-spectra in the spectral range from 3800–550 cm^{-1} of the catalyst layers of an as prepared MnO_x/CFP-electrode (purple line) and MnO_x/CFP-electrodes treated for 24 h at a constant current density of $j = 2$ mA cm^{-2} in 1 M KP_i-buffers of pH 2.5 (black), pH 7.0 (red) and pH 12.0 (blue), respectively.

1120 and 960 cm^{-1}, which have an especially high intensity for electrodes operated in pH 7.0 and 2.5, but are also clearly visible for the pH 12-sample. The origin of these features is most likely the incorporation of phosphate ions into the porous and layered birnessite material, as $H_nPO_4^{(3-n)-}$ species show prominent absorption bands in this spectral region (see ATR-IR-spectra of KH_2PO_4, K_2HPO_4 and K_3PO_4 shown in Fig. S9 of the ESI†).[75,76] These adsorbed phosphates are most likely only slowly exchangeable, as all electrodes were thoroughly washed with deionised water for several minutes after electrolysis to avoid surface contamination by K^+ and $H_nPO_4^{(3-n)-}$ from the electrolytes. The intensity differences found for the phosphate features can be seen as an indicator that the interaction between the manganese oxide catalyst and the phosphate anions is maximal under neutral conditions. In basic media, the smaller amount of bound $H_nPO_4^{(3-n)-}$ might be explained by competition with OH^- for anion binding sites of the birnessite catalyst material, which is inline with the especially strong OH^- stretching vibrations above 3000 cm^{-1} for the pH 12.0 sample.

Raman measurements largely confirmed the information obtained from the ATR-IR-spectra. Three major features ν_3, ν_2 and ν_1, all typical for birnessites, are detected at ~500, 570 and 655 cm^{-1} (see ESI, Fig. S10†).[73,77,78] No significant shifts of the positions of these bands were detected post *operando* between

the as-prepared electrodes and electrodes that had been used as OER-anodes. On the other hand, clear differences induced by the sintering step which is part of the preparation procedure are visible in the Raman spectra and interestingly indicate an increased disorder of the layers induced by the heating step. The Raman peaks for the sintered and operated electrodes are clearly broadened compared to those of a freshly prepared electrode dried at 60 °C. Such a band broadening of ν_2 and ν_1 can be ascribed to an increasing Jahn–Teller disorder within the [MnO_6]-octahedra.[79,80] Additionally, the intensity ratio $I(\nu_2)/I(\nu_1)$ of the two most intense bands shows a clear decrease from around 1.8 for freshly prepared electrodes compared to around 0.9 for activated electrodes and electrodes used as OER-anodes. This observation can be assigned to a decrease of the interlayer distance most likely due to the elimination of water from the birnessite interlayers during sintering.[77,81] After sintering has been carried out, the Raman results again indicate that there are only small structural differences post *operando* and that *e.g.* the incorporation of $H_nPO_4^{(3-n)-}$ into the catalyst detected by IR has no major influence on the bulk birnessite-type MnO_x structure. However, no additional Raman vibrations or reflexes attributable to $H_nPO_4^{(3-n)-}$ were observed, most likely due to the low Raman-scattering resonance enhancement for phosphate ions.[74]

EDX measurements proved to be an even better tool to confirm the ion-exchange processes during electrolysis than IR, as a post *operando* EDX-signal assignable to phosphorous confirms the phosphate uptake from the electrolyte (see ESI, Fig. S11–S14†). The detected phosphorous contents observed by EDX also nicely match the ATR-IR spectra, as the highest P : Mn-ratio is again found for the electrode tested at pH 7.0 (0.10 : 1) followed by the value for pH 2.5 (0.07 : 1) and the lowest number for pH 12.0 (0.05 : 1). Additionally, EDX also reveals an incorporation of additional potassium cations from the buffer media. Starting from a K : Mn ratio of approximately 0.05 : 1 for freshly prepared electrodes, we find that this value increases two- to four-fold during electrolysis to 0.10–0.20 K^+ ions per Mn after operation. Thus, both $H_nPO_4^{(3-n)-}$ anions and K^+ cations are adsorbed by the birnessite catalyst from the potassium phosphate buffer used as electrolyte.

XRD experiments are a useful tool to confirm the integrity of the carbon material, as the three most pronounced reflections in the XRD patterns (Fig. S15†) at $2\theta \sim 26°$, ~54° and ~86° are attributable to the (002), (004) and (006) planes of the graphitic electrode substrate, respectively. Additionally, the much less intense reflections at $2\theta \sim 12°$, ~37°, ~60° and ~77° are characteristic for the mostly amorphous/micro-crystalline birnessite material.[36,82] The absence of the (100) reflection at $2\theta \sim 12°$ for the calcinated electrode in comparison to the freshly prepared MnO_x/CFP dried at 60 °C again indicates a disordering of the stacking of the [MnO_6]-octahedral sheets through the heating step, as this is typically the XRD reflex with the highest intensity for birnessites.[83]

In addition to the data presented so far, much more detailed information concerning the structural and electronic properties of the materials could be extracted from X-ray absorption spectroscopy (XAS) experiments which were conducted at the KMC 3 beamline of the BESSY synchrotron in Berlin. XAS is an element-specific method not restricted to crystalline (like XRD) or specific electronic states (like NMR and EPR), or the presence of Mössbauer nuclei, and can be applied to almost any material under nearly any environmental conditions. It is thus especially suited to analyse amorphous transition metal oxides like birnessites and has been successfully used in this context by our groups before.[20,21,37,42,84]

Accordingly, X-ray absorption near-edge structure (XANES) and extended X-ray absorption fine structure (EXAFS) spectra at the Mn K-edge were recorded for freshly prepared MnO_x/CFP-electrodes (dried at 60 °C), after subsequent calcination at 400 °C, and again after operation for 24 h at the three pH values studied before in order to determine the average oxidation states and local coordination environments of the manganese

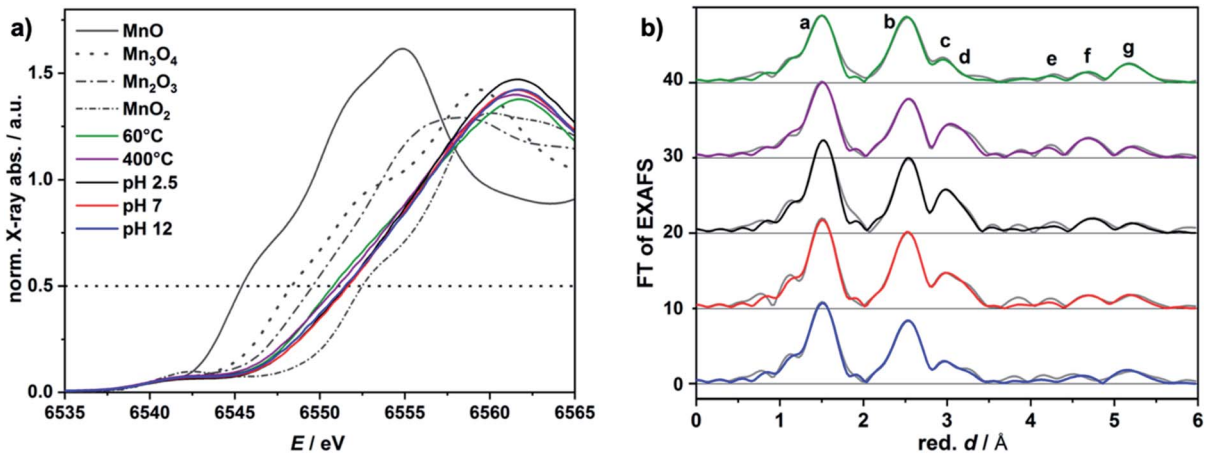

Fig. 5 (a) Mn K-edge XANES spectra of reference MnO_x powders (grey) and MnO_x/CFP-electrodes (in color) pre and post *operando* as WOC anodes in phosphate buffers of different pH. The horizontal line at 0.5 was used for the determination of the average Mn oxidation states (see Fig. S16 of the ESI†); (b) Fourier transform of the EXAFS spectra ((a)–(g) denote different backscattering atomic shells fitted as described in the main text).

ions in the catalyst materials. The XANES spectra measured for these five samples are displayed in Fig. 5a together with spectra of reference MnO_x powders of known oxidation states: $Mn^{II}O$, $Mn^{II}Mn_2^{III}O_4$, $Mn_2^{III}O_3$, and $Mn^{IV}O_2$. As previously observed for birnessite-type Mn oxides, all deposited samples show a small pre-edge feature and a shallow edge rise up to a level of normalized absorption of about 1.5.[21] The high degree of similarity for all electrodes in comparison to the much more pronounced differences between those recorded for the reference oxides suggests conserved structural properties as well as comparatively minor changes in the mean Mn oxidation state caused by electrochemical operation. The X-ray energy values at a normalized absorption of 0.5 (dotted horizontal line in Fig. 5a) of the reference compounds were used to determine the average Mn oxidation states for the electrodes (Fig. S16 of the ESI†). As anticipated from the very similar XANES spectra, these numbers vary only within a rather narrow range from 3.4 (for the fresh electrode dried at 60 °C), *via* 3.5 (after sintering at 400 °C) to 3.6–3.7 (after operation as OER electrocatalyst). On the other hand, if only $Mn^{3+} \rightarrow Mn^{4+}$ transitions are assumed, an Mn oxidation state increase by 0.1 corresponds to the oxidation of 10% of all Mn ions in the material and is thus very significant. The XANES data thus nicely supports our interpretation of the CV experiments (Fig. 2a), where the "pre-waves" observed at ~1.2–1.6 V indicated Mn-based redox activity for all three pH regimes. We would also like to mention that similar oxidation state changes have been found before for other birnessite samples exposed to OER conditions.[20,43,57]

EXAFS contains more detailed information about the local Mn coordination environment. For an analysis of the EXAFS data, the experimental spectra are usually fitted in *k*-space with a model of backscattering atomic shells (see Fig. S16†), and the Fourier-transform (FT) of the EXAFS is used to determine the geometric distances between the Mn centres and these scattering shells. Here, all five catalyst electrodes were modelled using seven shells around Mn which are labelled as (a)–(g) in Fig. 5b (see also Tables S1 and S2 of the ESI†). The Debye–Waller factors of the five outer shells were pre-fitted in alternation to the shell distances and finally kept constant at proper values.

All EXAFS spectra show two prominent peaks at about 1.90 and 2.88 Å, which stem from first-shell Mn–O and second-shell Mn–$(\mu\text{-O})_2$–Mn backscattering, as well as numerous smaller peaks between 3 and 6 Å. The distances of peaks (a) and (b) suggest O–Mn–O angles of ~80° and respective reciprocal O–M–O angles of ~100° for the interconnection of the $[MnO_6]$ moieties. This is in good agreement with the angles of ~85–95° known for crystalline K-rich birnessite, which was used as parent structure for the analysis.[85] Small changes of the atomic coordinates from this ideal birnessite arrangement already provide a variety of additional, nearby Mn–O and Mn–Mn distances, which can explain the peaks (c)–(g) in the EXAFS and might be visualised by the XAS-derived structural model for the deposited material shown in Fig. 6.

Additional structural information can be gathered from the longer Mn–Mn distances that are resolved in the EXAFS spectra. For example, a prominent far distanced peak at ~5.2 Å can be observed for the freshly deposited, mildly dried material

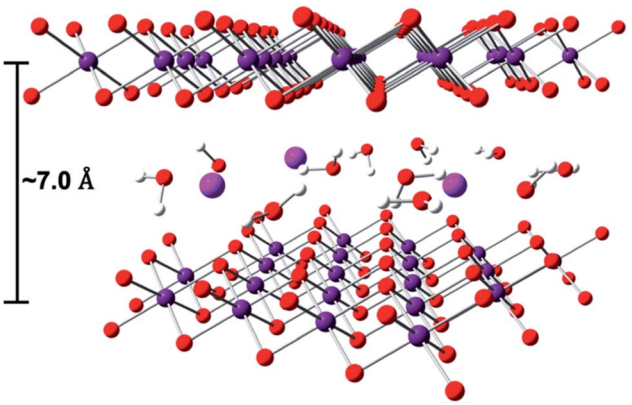

Fig. 6 Structural model of the deposited compounds derived from the crystal structure of K-rich birnessite[85] artificially "amorphized" by small random shifts of the ion coordinates. Colour code: red: oxygen; purple: manganese; pink: potassium; white: hydrogen.

(Fig. 5b, green curve, peak (g)), suggesting a considerable degree of long-range order for the oxide at this stage. In line with the observations made before using Raman spectroscopy and XRD, the intensity of this signal is markedly reduced by the calcination step at 400 °C, thus confirming that heating the oxide to this temperature indeed leads to an amorphization of the material. As a previous study on MnO_x/CFP-electrodes clearly showed that sintering at >200 °C is necessary to prepare electrodes of good electrochemical activity, the heating step thus represents another example of a "structural activation" of a birnessites-type material for WOC, as has already been described elsewhere.[43] As another interesting observation, the EXAFS spectrum of the electrode operated at pH 2.5 is hardly changed from that of the calcined material (see Fig. 5b, purple and black lines, peaks (e)–(g)), whereas this region of the EXAFS spectrum of the material operated at pH 12.0 is closer to that of the initial material dried at 60 °C (see Fig. 5b, green and blue lines, peaks (e)–(g)). The spectrum after operation at pH 12.0 thus suggests a re-ordering process, which may involve the formation of clusters of locally well ordered birnessites moieties. The red-coloured EXAFS spectrum of the electrode used for WOC at pH 7.0 in Fig. 5 has a shape in between that for the two pH extremes of pH 2.5 and pH 12.0 and may represent the transformation between these structures.

In conclusion, no major structural changes between the as-prepared MnO_x/CFP-electrodes after sintering and electrodes used for electrochemical WOC in media of pH 2.5/7.0/12.0 were uncovered by ATR-IR-, XAS-, Raman-, XRD- or SEM measurements, so that the studied anodes can be characterized as stable and catalytically active over this wide pH range. EDX and IR-measurements revealed that ion-exchange processes accompany the operation of the electrodes in phosphate buffers at all three pH regimes. However, neither the incorporation of phosphate or potassium ions from the electrolyte nor the slight increase of the average Mn oxidation state detected by XANES results in major structural changes for the birnessites-type materials. On the other hand, Raman, XRD and EXAFS revealed that the calcination step at 400 °C during preparation

induces a pronounced amorphization of the material and this might explain the higher activity of the thus "activated" compared to freshly prepared electrodes.

Influence of the solution pH on the catalytic activity

The dependence of the OER activity on the H^+/OH^--concentration was determined by performing steady-state stepwise chronoamperometric measurements at a constant phosphate concentration of 1.0 M by varying the pH of the solution from 1.5–13.0. The resulting *j vs. E* traces were used to generate Tafel-plots (see ESI, Fig. S17†) which show a clearly linear behaviour over two orders of magnitude of j (0.1–10 mA cm^{-2}). The potential E needed to achieve a current density of 200 μA cm^{-2} (Fig. 7a) shows a nearly constant value of $E = 1600$ mV *vs.* RHE over a large pH range from ~1.5 to ~10. However, for pH ~ 11–13 a quite dramatic shift to lower values ($E = 1530$ mV for pH 13.0) was observed, meaning that for strongly alkaline solutions much lower overpotentials are needed to achieve the same reaction rate. A similar trend is reflected by the Tafel slopes, where a decrease from ~150 mV dec^{-1} for pH 1.5 to ~40 mV dec^{-1} for pH 13.0 (Fig. 7b) was detected. Between pH 3 and 10, the Tafel slope is almost constant and close to $2 \cdot 59 = 118$ mV dec^{-1}, which is typical for multi-step reactions where the first oxidation is turnover-limiting.[86,87] However, between pH 10.0 to 13.0 the slope decreases drastically down to 40 mV dec^{-1}, suggesting a change of the rate determining step (RDS) and thus a different WOC mechanism. This low Tafel slope is characteristic of a multi-step reaction where a second potential-independent step is rate-determining,[86,88] and was also observed for a MnO_x/CFP-electrode tested in 1 M KOH-solution (see Fig. S18 in the ESI†).

This difference in the behaviour of MnO_x/CFP in the pH regime from 1.5–10.0 and 11.0–13.0 is also visible when the potentials E_{NHE} needed to achieve current densities of 1 or 5 mA cm^{-2}, respectively, are plotted against the pH (Fig. 7c). Linear regressions of the resulting current density values show the dependence of the potential E_{NHE} as a function of the pH. Interestingly, these lines do not show the same slope over the entire pH range. Instead, for pH < 10, slopes of −59 and −64 mV pH^{-1} (for 1 and 5 mA cm^{-1}, respectively) were found, which point at a Nernstian behaviour for a proton-coupled electron transfer (PCET) process with $n(H^+) : n(e^-) = 1 : 1$.[88] Above pH ~ 10, a marked change of the pH dependence is discernible resulting in slopes as low as −104 and −120 mV pH^{-1} (and thus closer to 2×59 mV pH^{-1}). Therefore, here a proton to electron ratio of two to one seems to be valid. The described shift from Nernstian behaviour to the mentioned deviation for pH > 10 is also visible in the onset of the OER in CV-experiments (Fig. 7d). On the RHE-scale, the detection of catalytic OER-currents starts

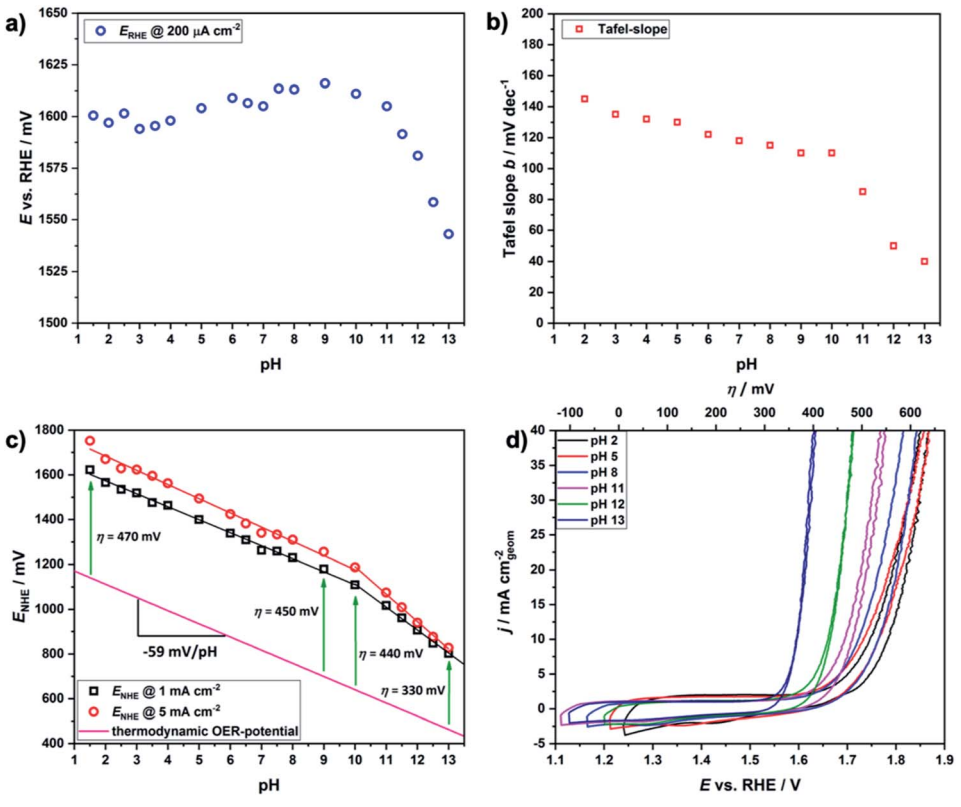

Fig. 7 (a) potential *E vs.* RHE needed to achieve a current density $j = 200$ μA cm^{-2} and change of the Tafel slope b (b) for different pH values; (c) potential E_{NHE} of MnO_x/CFP-electrodes needed to achieve a current density of 1 mA cm^{-2} (black open squares) and 5 mA cm^{-2} (red open dots) in 1 M KP_i-buffer in the pH range from 1.5–13.0. Additionally, the thermodynamic potential of the OER with respect to the pH is illustrated (pink line). The green arrows show the overpotential η that is needed to reach a current density $j = 1$ mA cm^{-2} for some pH values; (d) CVs recorded for MnO_x/CFP-electrodes in 1 M KP_i-buffer and variation of the pH.

more or less at the same potential for pH 1.5–10.0. However, above pH ~ 10, a shift to much lower onset potentials is observed. A very similar behaviour was found by Takashima *et al.* for spray-deposited δ-MnO_2 on FTO-glass slides and was explained by the higher stability of the Mn^{3+}-state under alkaline conditions.[47]

Non-ideal Nernstian pH-dependencies like the one found here for MnO_x/CFP are well known for more than three decades for the oxidations of metal surfaces in alkaline solutions (*e.g.* Ni, Ir, Rh, Fe).[89–92] Until now, no satisfactory explanation for this phenomena has been found, but a number of authors propose that the "super-Nernstian" shifts can be attributed to the adsorption of additional hydroxides on the material's surface. This could be achieved by direct OH^- incorporation from the bulk solution, a loss of protons from coordinated water molecules or the formation of hydroxyl complexes.[92–95] The thus formed negatively charged oxygen moieties are thought to be crucial for WOC, as a reaction of such species with other neighbouring OH-ligands or hydroxide ions from the electrolyte could lead to the more facile formation of reactive oxyl radical- (Mn–O$^\bullet$) or peroxido- (Mn–O–O–H, Mn–O–O$^-$) intermediates and hence to a higher WOC activity.[96–98] The formation of oxygen ligands with a formal oxidation state of −1 at high catalytic potentials was recently reported not only for NiFe oxides[14,99] but also concluded from *in situ* XAS spectroscopy for birnessite MnO_x.[100]

From the results presented in this section, we can draw some general conclusions concerning WOC by MnO_x/CFP-electrodes under different pH conditions: (1) from the Tafel data analysis it is obvious that a change of the mechanism from acidic/intermediate pHs to strongly alkaline conditions takes place. This leads to enhanced reaction rates for pH > 10; (2) accordingly, the OER onset potentials shift to lower values on the RHE scale, resulting in a super-Nernstian shift of the potential. This means that the ability to evolve oxygen is thermodynamically and kinetically favoured under strongly alkaline conditions, so that less energy is needed. Since super-Nernstian shifts can most likely be explained by the accumulation of negatively charged oxygen groups on the surface of the catalyst, we conclude that this could account for the more efficient water oxidation under alkaline conditions. Nevertheless, it appears difficult to make more detailed statements about the WOC mechanism for MnO_x/CFP without further evidences *e.g.* from *in situ* spectroscopic measurements.

Conclusions

This study shows that birnessite-coated carbon fibre papers (MnO_x/CFP) are efficient and stable anodes for electrocatalytic water oxidation over nearly the entire aqueous pH regime (pH 1–14). Furthermore, we observe that MnO_x/CFP is a volume catalyst where the electrocatalytic activity scales with the number of deposited Mn-ions. However, the dependence of catalytic current *vs.* n_{Mn} shows a saturation behaviour, which indicates that not all Mn ions contribute equally to the overall activity of the catalyst layer. Hence, as true mass transport limitations by the 'substrate water' or 'product O_2' are unlikely to be severe, charge transport limitations of protons/electrons to/away from the electrode seem to be major issues limiting the performance of electrodes with thicker MnO_x coatings. Accordingly, it might be possible to increase the activity of this catalyst system further by optimizing the electrical conductivity or charge transfer properties in general, *e.g.* by doping the MnO_x with suitable d-block cations.

Mass optimized electrodes (coated with ~3 μmol(Mn) per cm^2) showed remarkable activities and stabilities over the entire pH range. Even in acidic electrolytes, benchmark current densities of 1 or 5 mA cm^{-2} could be reached at overpotentials η between 350–550 mV. For electrodes that only contain the earth-abundant elements Mn, O and C, these values are among the best that have so far been published. Catalyst corrosion became detectable for electrodes operated at pH 7.0 or below, as ~1% of the total Mn dissolved in the form of permanganate, which could be identified spectroscopically as major corrosion product. On the other hand, no substantial Mn-loss was detected even after 24 h of continuous electrolysis, which indicates that the permanganate is re-deposited as birnessite over time, thus resulting in a rather stable WOC activity overall. No MnO_4^- formation was found for electrodes operated under more alkaline conditions.

The described activity and stability differences found for electrodes operated between pH 1–10 and those studied above pH 10 are most likely accompanied by a change of the reaction mechanism, indicated by a marked decrease of the Tafel slope as well as a transition from an ideal to a non-ideal Nernstian pH-dependence once the pH of the phosphate electrolyte is increased above ~pH 10. Hence, water-oxidation catalysis by MnO_x/CFP is kinetically and thermodynamically favoured under strongly alkaline conditions for so-far unknown reasons. However, very similar observations have been made for electrochemical WOC by Co- or Ni-oxides, suggesting that some general underlying principle might exist.

The stability of MnO_x/CFP over this very wide pH range was further confirmed by detailed pre- and post-*operando* spectroscopic analyses. No change in the morphology and only slight changes in the average Mn oxidation state or the oxide's composition were revealed after electrochemistry although some ion-exchange processes were taking place during operation. EXAFS measurements disclose only minor structural changes for the electrodes operated under different pH conditions, verifying the universal applicability of MnO_x/CFP.

Motivated by the very encouraging results of the presented study, we will continue to improve the electrocatalytic activities and stabilities of MnO_x/CFP-anodes, putting a special focus on the neutral to acidic pH regimes. For example, the incorporation of other transition metals, *e.g.* Co, Ni or Fe could improve the electrical conductivity of the birnessite coating and additional efforts could be made to further increase the surface area of the MnO_x/CFP hybrid. Looking ahead towards the construction of devices, we see possible applications of our catalyst system in PEM electrolysers and/or microbial electrosynthesis cells, both of which are usually operated at pH ≤ 7. Furthermore, *in situ* spectroscopy *during* electrochemical operation at different pH's could be carried out to (1) obtain additional

information concerning the oxygen evolution mechanism and (2) possibly solve the so far unclear origin of the differences in electrocatalytic performances between the pH < 10- and pH > 10-regimes.

Conflicts of interest

There are no conflicts to declare.

Acknowledgements

We gratefully acknowledge financial support by the German research foundation (Deutsche Forschungsgemeinschaft, DFG) within the priority program *SolarH$_2$* (SPP1613, grants KU2885/2-2 and DA402/7-2). J. M., P. H., R. L. and Ph. K. would also like to acknowledge funding by the Federal Ministry of Education and Research (BMBF, cluster project *MANGAN*, FKZ 03SF0511A), while S. M. and H. D. profited additionally from support from the DFG cluster *UniSysCat* (under Germany's Excellence Strategy, EXC 2008/1 – 390540038). We would also like to thank Prof. Dr Anna Fischer at the ALU Freiburg for the possibility to carry out electron microscopy at an BMBF founded HR-SEM instrument (project EDELKAT, FKZ 03X5524). Raman spectra were recorded at the Fraunhofer ISE/Freiburg in cooperation with Jörg Bierbaum and Daniel Philipp.

Notes and references

1 H. Dau, E. Fujita and L. Sun, *ChemSusChem*, 2017, **10**, 4228–4235.
2 D. G. Nocera, *Acc. Chem. Res.*, 2012, **45**, 767–776.
3 D. G. Nocera and N. S. Lewis, *Proc. Natl. Acad. Sci. U. S. A.*, 2006, **103**, 15729–15735.
4 N. Armaroli and V. Balzani, *Angew. Chem., Int. Ed.*, 2007, **46**, 52–66.
5 L. Sun, L. Hammarström, B. Åkermark and S. Styring, *Chem. Soc. Rev.*, 2001, **30**, 36–49.
6 M. W. Kanan and D. G. Nocera, *Science*, 2008, **321**, 1072–1075.
7 D. Gust, T. A. Moore and A. L. Moore, *Acc. Chem. Res.*, 2009, **42**, 1890–1898.
8 J. Melder, P. Bogdanoff, I. Zaharieva, S. Fiechter, H. Dau and P. Kurz, *Z. Phys. Chem.*, submitted.
9 N.-T. Suen, S.-F. Hung, Q. Quan, N. Zhang, Y.-J. Xu and H. M. Chen, *Chem. Soc. Rev.*, 2017, **46**, 337–365.
10 E. L. Miller and R. L. Rocheleau, *J. Electrochem. Soc.*, 1997, **144**, 3072.
11 A. Ursua, L. M. Gandia and P. Sanchis, *Proc. IEEE*, 2012, **100**, 410–426.
12 A. M. Smith, L. Trotochaud, M. S. Burke and S. W. Boettcher, *Chem. Commun.*, 2015, **51**, 5261–5263.
13 B. M. Hunter, J. D. Blakemore, M. Deimund, H. B. Gray, J. R. Winkler and A. M. Müller, *J. Am. Chem. Soc.*, 2014, **136**, 13118–13121.
14 S. Loos, I. Zaharieva, P. Chernev, A. Lißner and H. Dau, *ChemSusChem*, 2019, **12**, 1966–1976.
15 G. P. Gardner, Y. B. Go, D. M. Robinson, P. F. Smith, J. Hadermann, A. Abakumov, M. Greenblatt and G. C. Dismukes, *Angew. Chem., Int. Ed.*, 2012, **51**, 1616–1619.
16 M. Dincă, Y. Surendranath and D. G. Nocera, *Proc. Natl. Acad. Sci. U. S. A.*, 2010, **107**, 10337–10341.
17 D. K. Bediako, B. Lassalle-kaiser, Y. Surendranath, J. Yano, V. K. Yachandra and D. G. Nocera, *J. Am. Chem. Soc.*, 2012, **134**, 6801–6809.
18 Y. Wu, M. Chen, Y. Han, H. Luo, X. Su, M. T. Zhang, X. Lin, J. Sun, L. Wang, L. Deng, W. Zhang and R. Cao, *Angew. Chem., Int. Ed.*, 2015, **54**, 4870–4875.
19 M. Chen, Y. Wu, Y. Han, X. Lin, J. Sun, W. Zhang and R. Cao, *ACS Appl. Mater. Interfaces*, 2015, **7**, 21852–21859.
20 I. Zaharieva, P. Chernev, M. Risch, K. Klingan, M. Kohlhoff, A. Fischer and H. Dau, *Energy Environ. Sci.*, 2012, **5**, 7081–7089.
21 S. Y. Lee, D. González-Flores, J. Ohms, T. Trost, H. Dau, I. Zaharieva and P. Kurz, *ChemSusChem*, 2014, **7**, 3442–3451.
22 J. Melder, W. L. Kwong, D. Shevela, J. Messinger and P. Kurz, *ChemSusChem*, 2017, 4491–4502.
23 C. C. L. McCrory, S. Jung, I. M. Ferrer, S. Chatman, J. C. Peters and T. F. Jaramillo, *J. Am. Chem. Soc.*, 2015, **137**, 4347–4357.
24 L. C. Seitz, C. F. Dickens, K. Nishio, Y. Hikita, J. Montoya, A. Doyle, C. Kirk, A. Vojvodic, H. Y. Hwang, J. K. Norskov and T. F. Jaramillo, *Science*, 2016, **353**, 1011–1014.
25 K. Sun, I. A. Moreno-Hernandez, W. C. Schmidt, X. Zhou, J. C. Crompton, R. Liu, F. H. Saadi, Y. Chen, K. M. Papadantonakis and N. S. Lewis, *Energy Environ. Sci.*, 2017, **10**, 987–1002.
26 A. Minguzzi, F.-R. F. Fan, A. Vertova, S. Rondinini and A. J. Bard, *Chem. Sci.*, 2012, **3**, 217–229.
27 M. Carmo, D. L. Fritz, J. Mergel and D. Stolten, *Int. J. Hydrogen Energy*, 2013, **38**, 4901–4934.
28 F. Barbir, *Sol. Energy*, 2005, **78**, 661–669.
29 H. Dau and I. Zaharieva, *Acc. Chem. Res.*, 2009, **42**, 1861–1870.
30 N. Cox, D. A. Pantazis, F. Neese and W. Lubitz, *Acc. Chem. Res.*, 2013, **46**, 1588–1596.
31 J. Yano and V. Yachandra, *Chem. Rev.*, 2014, **114**, 4175–4205.
32 J. Barber, *Chem. Soc. Rev.*, 2009, **38**, 185–196.
33 I. Vass and S. Styring, *Biochemistry*, 1991, **30**, 830–839.
34 N. Cox and J. Messinger, *Biochim. Biophys. Acta*, 2013, **1827**, 1020–1030.
35 V. Krewald, M. Retegan, N. Cox, J. Messinger, W. Lubitz, S. DeBeer, F. Neese and D. A. Pantazis, *Chem. Sci.*, 2015, **6**, 1676–1695.
36 C. E. Frey and P. Kurz, *Chem.–Eur. J.*, 2015, **21**, 14958–14968.
37 I. Zaharieva, M. M. Najafpour, M. Wiechen, M. Haumann, P. Kurz and H. Dau, *Energy Environ. Sci.*, 2011, **4**, 2400.
38 R. K. Hocking, R. Brimblecombe, L.-Y. Chang, A. Singh, M. H. Cheah, C. Glover, W. H. Casey and L. Spiccia, *Nat. Chem.*, 2011, **3**, 461–466.
39 A. Ramírez, D. Friedrich, M. Kunst and S. Fiechter, *Chem. Phys. Lett.*, 2013, **568–569**, 157–160.

40 Y. Meng, W. Song, H. Huang, Z. Ren, S. Chen and S. L. Suib, *J. Am. Chem. Soc.*, 2014, **136**, 11452–11464.
41 D. M. Robinson, Y. B. Go, M. Mui, G. Gardner, Z. Zhang, D. Mastrogiovanni, E. Garfunkel, J. Li, M. Greenblatt and G. C. Dismukes, *J. Am. Chem. Soc.*, 2013, **135**, 3494–3501.
42 M. Wiechen, I. Zaharieva, H. Dau and P. Kurz, *Chem. Sci.*, 2012, **3**, 2330.
43 D. González-Flores, I. Zaharieva, J. Heidkamp, P. Chernev, E. Martínez-Moreno, C. Pasquini, M. R. Mohammadi, K. Klingan, U. Gernet, A. Fischer and H. Dau, *ChemSusChem*, 2016, **9**, 379–387.
44 J. E. Post, *Proc. Natl. Acad. Sci. U. S. A.*, 1999, **96**, 3447–3454.
45 A. Ramírez, P. Hillebrand, D. Stellmach, M. M. May, P. Bogdanoff and S. Fiechter, *J. Phys. Chem. C*, 2014, **118**, 14073–14081.
46 C. Walter, P. W. Menezes, S. Loos and H. Dau, *ChemSusChem*, 2018, 2554–2561.
47 T. Takashima, K. Hashimoto and R. Nakamura, *J. Am. Chem. Soc.*, 2012, **134**, 1519–1527.
48 London Metal Exchange, https://www.lme.com, accessed 25 June 2019.
49 C. E. Frey, M. Wiechen and P. Kurz, *Dalton Trans.*, 2014, **43**, 4370–4379.
50 H. Dau and C. Pasquini, *Inorganics*, 2019, **7**, 1–11.
51 S. Levine and A. L. Smith, *Discuss. Faraday Soc.*, 1971, **52**, 290.
52 C. C. L. McCrory, S. Jung, J. C. Peters and T. F. Jaramillo, *J. Am. Chem. Soc.*, 2013, **135**, 16977–16987.
53 S. Trasatti and O. A. Petrii, *Pure Appl. Chem.*, 1991, **63**, 711–734.
54 H.-W. Chang, Y.-R. Lu, J.-L. Chen, C.-L. Chen, J.-F. Lee, J.-M. Chen, Y.-C. Tsai, P.-H. Yeh, W. C. Chou and C.-L. Dong, *Phys. Chem. Chem. Phys.*, 2016, **18**, 18705–18718.
55 W. Wei, X. Cui, W. Chen and D. G. Ivey, *Chem. Soc. Rev.*, 2011, **40**, 1697–1721.
56 A. Bergmann, I. Zaharieva, H. Dau and P. Strasser, *Energy Environ. Sci.*, 2013, **6**, 2745–2755.
57 I. Zaharieva, D. González-Flores, B. Asfari, C. Pasquini, M. R. Mohammadi, K. Klingan, I. Zizak, S. Loos, P. Chernev and H. Dau, *Energy Environ. Sci.*, 2016, **9**, 2433–2443.
58 K. Klingan, F. Ringleb, I. Zaharieva, J. Heidkamp, P. Chernev, D. Gonzalez-Flores, M. Risch, A. Fischer and H. Dau, *ChemSusChem*, 2014, **7**, 1301–1310.
59 R. N. De Guzman, A. Awaluddin, Y. F. Shen, Z. R. Tian, S. L. Suib, S. Ching and C. L. O'Young, *Chem. Mater.*, 1995, **7**, 1286–1292.
60 S.-L. Kuo and N.-L. Wu, *J. Electrochem. Soc.*, 2006, **153**, A1317.
61 N. V. Klassen, D. Marchlngton and H. C. E. Mcgowan, *Anal. Chem.*, 1994, **66**, 2921–2925.
62 M. Huynh, C. Shi, S. J. L. Billinge and D. G. Nocera, *J. Am. Chem. Soc.*, 2015, **137**, 14887–14904.
63 M. Huynh, D. K. Bediako and D. G. Nocera, *J. Am. Chem. Soc.*, 2014, **136**, 6002–6010.
64 L. Han, P. Tang, Á. Reyes-Carmona, B. Rodríguez-García, M. Torréns, J. R. Morante, J. Arbiol and J. R. Galan-Mascaros, *J. Am. Chem. Soc.*, 2016, **138**, 16037–16045.
65 L. C. Seitz, C. F. Dickens, K. Nishio, Y. Hikita, J. Montoya, A. Doyle, C. Kirk, A. Vojvodic, H. Y. Hwang, J. K. Norskov and T. F. Jaramillo, *Science*, 2016, **353**, 197–203.
66 A. Yamaguchi, R. Inuzuka, T. Takashima, T. Hayashi, K. Hashimoto and R. Nakamura, *Nat. Commun.*, 2014, **5**, 4256.
67 Z. N. Zahran, E. A. Mohamed and Y. Naruta, *J. Mater. Chem. A*, 2017, **5**, 15167–15174.
68 M. W. Kanan and D. G. Nocera, *Science*, 2008, **321**, 1072–1075.
69 B. Zhang, Y. Li, M. Valvo, L. Fan, Q. Daniel, P. Zhang, L. Wang and L. Sun, *ChemSusChem*, 2017, **10**, 1–8.
70 M. W. Louie and A. T. Bell, *J. Am. Chem. Soc.*, 2013, **135**, 12329–12337.
71 F. Dionigi, T. Reier, Z. Pawolek, M. Gliech and P. Strasser, *ChemSusChem*, 2016, **9**, 962–972.
72 M. Gorlin, J. F. De Araujo, H. Schmies, D. Bernsmeier, S. Dresp, M. Gliech, Z. Jusys, P. Chernev, R. Kraehnert, H. Dau and P. Strasser, *J. Am. Chem. Soc.*, 2017, **139**, 2070–2082.
73 C. M. Julien, M. Massot and C. Poinsignon, *Spectrochim. Acta*, 2004, **60**, 689–700.
74 K. Nakamoto, *Infrared and Raman Spectra of Inorganic and Coordination Compounds Part A: Theory and Applications*, John Wiley & Sons, New Jersey, 6th edn, 2009.
75 R. L. Frost, Y. Xi, R. Scholz, A. López and F. M. Belotti, *Vib. Spectrosc.*, 2013, **66**, 69–75.
76 M. A. Woo, T. Woo Kim, M. J. Paek, H. W. Ha, J. H. Choy and S. J. Hwang, *J. Solid State Chem.*, 2011, **184**, 171–176.
77 C. Julien, M. Massot, R. Baddour-Hadjean, S. Franger, S. Bach and J. P. Pereira-Ramos, *Solid State Ionics*, 2003, **159**, 345–356.
78 F. Buciuman, F. Patcas, R. Craciun and D. R. T. Zahn, *Phys. Chem. Chem. Phys.*, 1999, **1**, 185–190.
79 R. E. Ruther, A. F. Callender, H. Zhou, S. K. Martha and J. Nanda, *J. Electrochem. Soc.*, 2014, **162**, A98–A102.
80 C. Julien and M. Massot, *Phys. Chem. Chem. Phys.*, 2002, **4**, 4226–4235.
81 D. Chen, D. Ding, X. Li, G. H. Waller, X. Xiong, M. A. El-Sayed and M. Liu, *Chem. Mater.*, 2015, **27**, 6608–6619.
82 S. Grangeon, B. Lanson and M. Lanson, *Acta Crystallogr.*, 2014, **70**, 828–838.
83 M. Villalobos, B. Toner, J. Bargar and G. Sposito, *Geochim. Cosmochim. Acta*, 2003, **67**, 2649–2662.
84 C. E. Frey, F. Kwok, D. González-Flores, J. Ohms, K. Cooley, H. Dau, I. Zaharieva, T. Walter, H. Simchi, S. Mohney and P. Kurz, *Sustainable Energy Fuels*, 2017, **1**, 1162–1170.
85 J. E. Post and D. R. Veblen, *Am. Mineral.*, 1990, **75**, 477–489.
86 E. Gileadi, *Electrode Kinetics for Chemists, Chemical Engineers and Materials Scientists*, VCH Publishers, Inc., Weinheim, 1st edn, 1993.
87 R. L. Doyle, I. J. Godwin, M. P. Brandon and M. E. Lyons, *Phys. Chem. Chem. Phys.*, 2013, **15**, 13737–13783.

88 L. R. Faulkner and A. J. Bard, *Electrochemical Methods: Fundamentals and Applications*, John Wiley & Sons, 2nd edn, 2001.
89 L. D. Burke, M. E. Lyons and D. P. Whelan, *J. Electroanal. Chem.*, 1982, **139**, 131–142.
90 L. D. Burke and M. B. C. Roche, *J. Electroanal. Chem.*, 1983, **159**, 89–99.
91 L. D. Burke and T. A. M. Twomey, *J. Electroanal. Chem.*, 1984, **167**, 285–290.
92 L. D. Burke and M. E. G. Lyons, in *Modern Aspects of Electrochemistry*, 1986, vol. 18, p. 169.
93 L. D. Burke, M. E. Lyons, E. J. M. O'Sullivan and D. P. Whelan, *J. Electroanal. Chem.*, 1981, **122**, 403–407.
94 L. D. Burke and D. P. Whelan, *J. Electroanal. Chem.*, 1981, **124**, 333–337.
95 L. D. Burke and T. A. M. Twomey, *J. Electroanal. Chem.*, 1982, **134**, 353–362.
96 M. Zhang, M. De Respinis and H. Frei, *Nat. Chem.*, 2014, **6**, 362–367.
97 O. Diaz-Morales, D. Ferrus-Suspedra and M. T. M. Koper, *Chem. Sci.*, 2016, **7**, 2639–2645.
98 B. J. Trześniewski, O. Diaz-Morales, D. A. Vermaas, A. Longo, W. Bras, M. T. M. Koper and W. A. Smith, *J. Am. Chem. Soc.*, 2015, **137**, 15112–15121.
99 D. Drevon, M. Görlin, P. Chernev, L. Xi, H. Dau and K. M. Lange, *Sci. Rep.*, 2019, **9**, 1532.
100 M. F. Tesch, S. A. Bonke, T. E. Jones, M. N. Shaker, J. Xiao, K. Skorupska, R. Mom, J. Melder, P. Kurz, A. Knop-Gericke, R. Schlögl, R. K. Hocking and A. N. Simonov, *Angew. Chem., Int. Ed.*, 2019, **58**, 3426–3432.